

Coastal Dune Erosion and Slumping Processes in the Swash-Dune Collision Regime Based on Field Measurements

van Wiechen, P. P. J.; Mieras, R.; Tissier, M. F. S.; Vries, S. de

DOI

[10.1029/2024JF007711](https://doi.org/10.1029/2024JF007711)

Publication date

2024

Document Version

Final published version

Published in

Journal of Geophysical Research: Earth Surface

Citation (APA)

van Wiechen, P. P. J., Mieras, R., Tissier, M. F. S., & Vries, S. D. (2024). Coastal Dune Erosion and Slumping Processes in the Swash-Dune Collision Regime Based on Field Measurements. *Journal of Geophysical Research: Earth Surface*, 129(10), Article e2024JF007711. <https://doi.org/10.1029/2024JF007711>

Important note

To cite this publication, please use the final published version (if applicable). Please check the document version above.

Copyright

Other than for strictly personal use, it is not permitted to download, forward or distribute the text or part of it, without the consent of the author(s) and/or copyright holder(s), unless the work is under an open content license such as Creative Commons.

Takedown policy

Please contact us and provide details if you believe this document breaches copyrights. We will remove access to the work immediately and investigate your claim.

Coastal Dune Erosion and Slumping Processes in the Swash-Dune Collision Regime Based on Field Measurements



Key Points:

- Field measurements of dune erosion rates and slumping volumes during two storms are related to hydrodynamic forcings
- Measured erosion rates at the dune base show strong correlations with the water level at the dune base
- The timing of slumps was related to the size of previous slumps and the erosion rates at the dune base

Correspondence to:




P. P. J. van Wiechen,
P.P.J.vanWiechen@tudelft.nl

Citation:

van Wiechen, P. P. J., Mieras, R., Tissier, M. F. S., & de Vries, S. (2024). Coastal dune erosion and slumping processes in the swash-dune collision regime based on field measurements. *Journal of Geophysical Research: Earth Surface*, 129, e2024JF007711. <https://doi.org/10.1029/2024JF007711>

Received 29 FEB 2024

Accepted 15 SEP 2024

P. P. J. van Wiechen¹ , R. Mieras², M. F. S. Tissier¹ , and S. de Vries¹ 

¹Department of Hydraulic Engineering, Delft University of Technology, Delft, The Netherlands, ²Department of Physics and Physical Oceanography, University of North Carolina Wilmington, Wilmington, NC, USA

Abstract This paper studies hydrodynamic and morphodynamic field measurements of two storms with dune erosion in the swash-dune collision regime. It analyses (a) the behavior and change of the total dune profile over the course of both storms (b) the erosion rate at the dune base, (c) the slumping frequency, and (d) the volumes of individual slumps. The erosion rate at the dune base shows a strong positive correlation with the square of the total water levels that were exceeded for 2% of the time, recorded approximately 5–6 m in front of the dune face ($r = 0.91$). Individual slumping events occurred when nearly all sediments from previous slumps at the dune base were transported away from the dune. A strong positive correlation was found between the time between two consecutive slumps, and the volume of the first slump divided by the mean erosion rate between the two slumps ($r = 0.90$). As a consequence, smaller slumps were followed more rapidly by a new slump than larger slumps, under identical erosion rates. The majority of the slumping events occurred after the last wave impact before a slumping event, when the instantaneous water level in front of the dune was still retreating. No clear process based on the incident hydrodynamics could be identified that determined the size of individual slumps. Overall, the results of this study suggest that the morphodynamic behavior of the upper dune face and dune crest is primarily steered by the erosion at the dune base.

Plain Language Summary At sandy coastlines, dunes often act as the primary sea defense against storms. During storms, an elevated water level temporarily submerges the beach, enabling waves to collide with the dune. In time, the dune becomes unstable and slumps of sediment periodically slide down the dune and drop at the dune base. Here, waves transport the sediment away, leaving room for a new slump to drop down. This paper analyses data from a field experiment and examines the speed with which sediment at the dune base eroded away. It studies when and what caused a slump to fall down, and what determined the size of slumps. The erosion speed with which sediments are transported away from the dune increased when the elevation difference between the incident water levels and the dune toe increased. The size of the previous slumps and the erosion speed of the slumped sediments at the dune base determined when a new slump dropped down. No clear explanation for the size of slumps could be found following from this study. Overall, the results of this study suggest that the erosion speed of the slumped sediments at the dune base steers the behavior of the upper dune.

1. Introduction

At sandy coastlines, dunes often act as the primary sea defense against storm surges with dune erosion in the swash-dune collision regime. In this regime, an elevated water level temporarily submerges the beach, allowing the incident swash to run up to the dunes and collide with the dune face (Ruggiero et al., 2001; Sallenger, 2000; Stockdon et al., 2006; van Thiel de Vries et al., 2007; van Wiechen, de Vries et al., 2023). The swash-dune collision regime limits itself to waves that reach the dune face, but that do not overtop the dune crest (for a full description of the swash-dune collision regime, see Sallenger, 2000). The impact of colliding waves results in significant erosion of the dune, with potential dune breaching and flooding of the hinterland as a consequence (Castelle et al., 2015; Leaman et al., 2021; Masselink et al., 2016; Vellinga, 1978). Knowledge of the underlying physical processes governing the hydro- and morphodynamics during dune erosion can increase capabilities to predict the impact of storm surges (Gharagozlou et al., 2020; Kobayashi et al., 2009; Roelvink et al., 2009, 2018; Steetzel, 1993; van Gent et al., 2008; Vellinga, 1986).

Slumping has been identified as one of the principle mechanisms that occur during dune erosion in the swash-dune collision regime (van Bemmelen et al., 2020; van Gent et al., 2008; van Wiechen, de Vries et al., 2023). Marine processes in front of the dune suspend sediment into the water column and transport the sediment away

© 2024. The Author(s).

This is an open access article under the terms of the [Creative Commons Attribution License](https://creativecommons.org/licenses/by/4.0/), which permits use, distribution and reproduction in any medium, provided the original work is properly cited.

from the dune. As a consequence, the dune face steepens. The collision of incident waves also results in the horizontal infiltration of water into the dune face due to capillary action, which enhances the cohesion of the dune sediments (Palmsten & Holman, 2011). As a result, the steepening of the dune face can continue until it has a nearly vertical or overhanging profile (Nishi et al., 1994). This new profile leads to an unstable situation which can eventually result in a slumping event. Erikson et al. (2007) studied dune instabilities leading up to slumping events for vertical dune faces. They defined the concept of notching (after a similar concept in Carter et al., 1990), where the vertical dune face was undercut by the removal of sediments from the dune base. This led to the formation of a notch that gradually increased in size. Notching eventually resulted in two types of mass failure of the dune: shear-type or beam-type failure. With shear-type failure, the weight of the overhanging sediment above the notch is too large and a slump drops down due to gravity. With beam-type failure, a tensile crack appears landward of the dune face, which initiates a slump of sediment to rotate or slide down the dune face.

The slumped sediments are deposited at the dune base, where they appear to temporarily obstruct further dune erosion by direct wave attack (van Gent et al., 2008). Still, incident waves gradually suspend the slumped sediments into the water column and transport them away from the dune base. This again steepens the dune and leaves the dune face exposed, forcing a new slump to drop or slide down in time. This cyclic behavior of slumping events can persist until the dune breaches and enters the overwash regime (Sallenger, 2000), and complete failure of the dune may follow.

Slumping processes and the resulting cumulative dune erosion volume have been related to (a) the impact of incoming waves (Erikson et al., 2007; Fisher et al., 1987; Larson et al., 2004; Overton et al., 1988, 1994), and (b) internal soil instabilities, where destabilizing forces within the beach and dune profile exceed stabilizing forces (Conti et al., 2024; Palmsten & Holman, 2011, 2012). Wave impact studies found a linear relation between the impact force of the incident wave and the eroded volume from the dune due to slumping. Soil instability studies found a relation between destabilizing forces, following from pore moisture content and the horizontal infiltration of water, and the erosion rate of the dune. Palmsten and Holman (2011) found that the infiltration of water increased the apparent cohesion of sediments, which allowed steeper slopes of the dune face. However, it ultimately led to soil failure because the total weight of the wetted block, kept together by the cohesion, exceeded the tensile strength of the soil. Conti et al. (2024) found that pore-water content can influence the rate of dune erosion, where the dune face receded more rapidly for higher moisture content cases.

Studies of wave impact theory and soil instabilities conducted up to now were mostly based on laboratory experiments or relatively calm field conditions, where the hydrodynamics were controlled and important mechanisms were monitored accurately (Bond et al., 2023; Conti et al., 2024; Overton et al., 1994; Palmsten & Holman, 2012). Several laboratory experiments were confined to analyses of a single slumping event (Erikson et al., 2007; Overton et al., 1988, 1994). Such experiments did not include the cyclic behavior of slumping, and the temporal contribution of a fallen slump to the obstruction of further dune erosion by direct wave attack. In addition, they did not study dune erosion and slumping processes over the course of a storm of several hours. Laboratory studies that did analyze the temporal behavior of dunes during a complete (simulated) storm often confined themselves to averaged offshore sediment transport rates, or average dune retreat (Feagin et al., 2023; Palmsten & Holman, 2011, 2012; van Gent et al., 2008; van Thiel de Vries et al., 2008). These studies did not conduct a slump-by-slump analysis, examining the volume of individual slumps.

Detailed field observations and measurements of dune erosion during energetic storm conditions often discuss total eroded volumes, and compare post-storm and pre-storm profile observations (de Winter et al., 2015; Schweiger et al., 2020; van Bemmelen et al., 2020). Field observations of the cyclic behavior of slumping and the frequency and size of individual slumps are rare due to (a) the unpredictability of storms, (b) the risks storms pose for instruments and observers, and (c) the difficulty of performing measurements in moderate to harsh hydrodynamic conditions. However, such observations and measurements are essential to understand and validate the magnitude and importance of dune erosion and slumping processes in more energetic field conditions and actual storm conditions.

This study uses and analyses hydrodynamic and morphodynamic data of a detailed dune erosion field experiment to study dune erosion rates and slumping processes. Two artificial unvegetated dunes with a crest height of 5.5 m NAP (Normaal Amsterdams Peil, the Dutch chart datum) were constructed above the high water line and monitored for 3 months (Rutten et al., 2024a; van Wiechen et al., 2024). Within this time span, three substantial storms occurred that resulted in dune erosion in the swash-dune collision regime with multiple slumping events

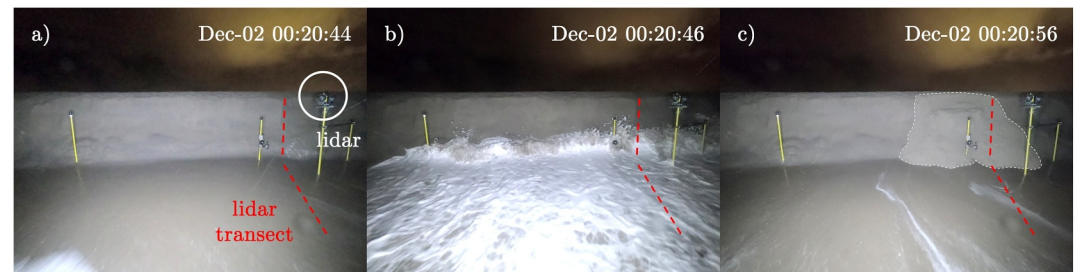


Figure 1. Dune face of the monitored dune during the storm in December 2021, (a) before wave impact, (b) during wave impact, and (c) shortly after wave impact. The slump displayed here is the largest registered slump of the December storm.

(Figure 1). The dune face of one dune was monitored with a line-scanning lidar system (O'Connor & Mieras, 2022) during two of the three storms, which allowed a detailed characterization of individual slumping events at this one dune over the course of these two storms. The first of these two storms occurred in December 2021 and had a water level with a return period of 0.2 years (Watermanagementcentrum Nederland, 2021). The second storm occurred in January 2022 and had a return period of 1.0 years (Watermanagementcentrum Nederland, 2022). No data were collected during the experiment about internal pore moisture content, pore pressures, and the distribution of destabilizing forces within the dune. Therefore, this study confines itself to studying the effect of hydrodynamic processes seaward of the dune on dune erosion rates and slumping processes.

First, the experiment, field site, and instrumentation are discussed in Section 2. Section 3 presents the methodology used to process the lidar data. Section 4 analyses (a) the behavior and change of the total dune profile due to both storms, (b) the erosion rate at the dune base during both storms, (c) the slumping frequency and the exact time at which a slumping event occurred, and (d) the volumes of individual slumps. The accuracy of the assumptions and results, and implications for dune erosion models are discussed in Section 5. Finally, conclusions are drawn in Section 6.

2. Field Site and Instrumentation

The data presented in this study were collected during the RealDune/REFLEX field experiments in the autumn of 2021 and winter of 2021–2022. Below, a summary is given of the segment of the field site and instrumentation that is relevant for this study. For a detailed description of the complete field site, experiment setup, instrumentation, and all collected data, the reader is referred to van Wiechen et al. (2024) and Rutten et al. (2024a). The local coordinate system and station numbers defined in van Wiechen et al. (2024) and Rutten et al. (2024a) have been adopted here to remain consistent.

The field site was located on the Sand Engine, a mega-nourishment near Kijkduin, the Netherlands (Stive et al., 2013). Two artificial unvegetated dunes with a crest height of 5.5 m NAP and 150 m wide were constructed above the high water line and observed for a period of 3 months. Within this time span, three storms passed that resulted in erosion of the dune face at both dunes. During two of these three storms, the dune face of one dune was monitored with a Line-scanning, Low-Cost (LLC) lidar system (for more information about this system see O'Connor & Mieras, 2022). This was the first full-scale field study to employ the use of this fully standalone, weather resistant, LLC lidar system. It performed approximately 6 rotations (i.e., scans) per second in the 2DV plane. Within a single rotation, the angular resolution was approximately 0.3° ; however, the angles at which range measurements were made is not consistent with each rotation, yielding an angular resolution greater than 0.3° over multiple scans. The point clouds of the scans were converted to cross-shore and elevation coordinates (NAP) using the lidar origin location and the 3D orientation of the instrument consisting of a yaw, pitch, and roll angle. Additional information about this conversion can be found in van Wiechen et al. (2024).

The accuracy of the LLC lidar system was assessed at the Field Research Facility in Duck, North Carolina, U.S.A., in O'Connor and Mieras (2022) by (a) comparing measured beach profiles at two different cross-shore locations by the LLC lidar system and a Riegl VZ-1000 system (O'Dea et al., 2019), and (b) comparing water levels derived from point clouds from the LLC lidar system with a co-located pressure sensor. Overall, the mean \pm standard deviation RMSD (root-mean squared difference) between the profiles measured by both lidar systems were $0.045 \text{ m} \pm 0.004 \text{ m}$, and $0.031 \text{ m} \pm 0.002 \text{ m}$, for the two cross-shore locations. The average RMSD between

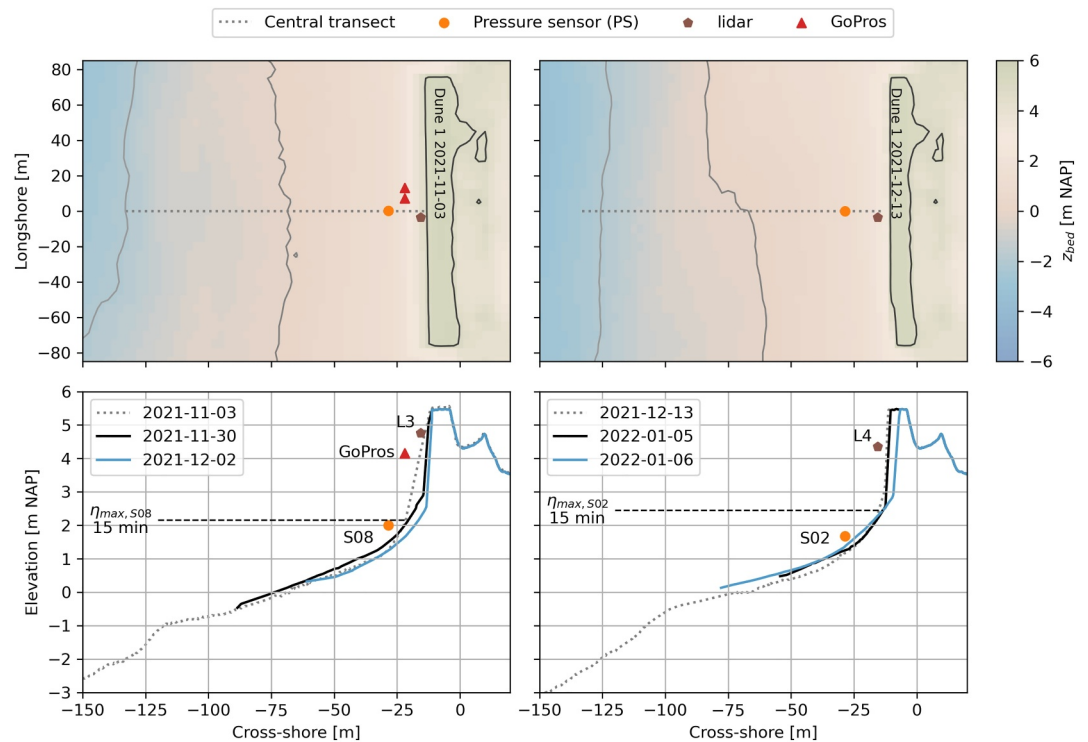


Figure 2. Instrumentation at Dune 1 during the December storm (left panels) and January storm (right panels). The bathymetries in the upper panels are based on detailed bathymetry and topography surveys conducted on November 3 and December 13. The lidar transect was approximately 1.5 m to the right (when facing the dune) of the central transect in the upper panels. Horizontal dashed lines in the lower panels represent the maximum mean (i.e., 15-min averaged) water levels recorded at S08 and S02 during the storms.

water levels derived from the LLC lidar system and pressure sensor was 0.027 m for ten 25-min time segments spanning 5 hr in the swash and inner surf-zones. Overall, the small RMSDs of both comparisons for the bathymetric and hydrodynamic data are smaller than the measured physical signal. Hereafter in this paper, the LLC lidar system will be referred to as “lidar.”

This study will focus on the two storm data sets at the dune where the lidar recorded the dune face (Dune 1). The first storm passed on December 2, where the mean (i.e., 15-min averaged) water level in front of the dune reached a maximum of 2.15 m NAP at 00:16 local time (Figure 2, lower left panel). The offshore sea swell wave height, $H_{m0,SS}$, was 2.59 m and period, $T_{m01,SS}$, was 7.19 s. The second storm passed on January 5, where the mean water level in front of the dune reached a maximum of 2.44 m NAP at 16:43 local time (Figure 2, lower right panel), with an offshore $H_{m0,SS}$ of 3.34 m and $T_{m01,SS}$ of 7.27 s. Hereafter in this paper, these storms will be referred to as the December storm and January storm.

The pre- and post-storm bathymetry and topography were recorded before and after the December and January storms (see black and blue lines in lower panels of Figure 2). During the December storm, one lidar system recorded the dune face (L3, left panels Figure 2). Lidar L3 captured the dune face up to 5.0 m NAP, not recording the upper 0.5 m of the dune face. During the January storm, one lidar system recorded the entire dune face (L4, right panels Figure 2), including the dune crest. In December, the lidar recorded in 35-min bursts every hour. In January, the lidar recorded in 50-min bursts every hour.

In addition to the lidar systems, nearshore pressure sensors and two nearshore GoPro cameras are used in this study. The pressure sensors were deployed at S08 in December and S02 in January, and recorded pressure at 8 Hz. The two GoPro cameras were only deployed during the December storm, and were installed near the dune face from 2021-12-01, 23:20, to 2021-12-02, 4:00. The GoPro cameras faced the dune face and recorded two frames every second. The lidar transect is within the frame of both GoPro cameras (Figure 1), and approximately 1.5 m to

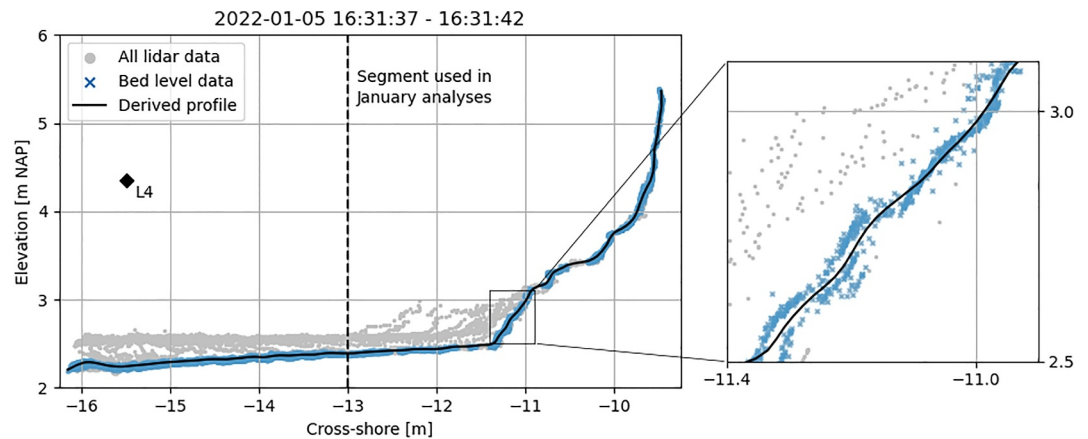


Figure 3. Total lidar point cloud for a 5 s bin during the January storm (gray and blue markers), separated bed level points (blue markers), and derived profile based on the separated bed level points (black).

the right (when facing the dune) of the central cross-section of the dune on which the pressure sensors at S08 (December) and S02 (January) were installed.

The sediments of the field site were sieved by the laboratory facilities of the University of Utrecht. The sediments were categorized as slightly gravelly sand, with a gravel content of 0.2% and sand content of 99.8%. The sediments had a D_{10} , D_{25} , D_{50} , D_{75} , and D_{90} of 236.0, 287.3, 362.3, 443.0, and 557.6 μm , respectively, where the subscript corresponds to the fraction of the sediments that had a grain size smaller than the value (i.e., 90% of the sediments had grain size smaller than 557.6 μm). No data are available about the compaction and porosity of the dune sediments.

3. Methodology

3.1. Lidar-Derived Dune Profiles

Variability within the unprocessed lidar point clouds was large due to the lidar recording both the water level and the bed level during a scan. Therefore, a detailed filtering procedure was required to extract points representing the bed, and use these filtered bed level points to compute dune profiles.

Points representing the bed were filtered from the translated and rotated point clouds using a standard deviation filter consisting of three steps. First, the data were binned in time bins of 5 s and angular bins of 1.5 times the angular resolution of each 35- or 50-min burst ($\approx 0.65^\circ$). Second, within each bin, all data points with a radius smaller than the mean minus the standard deviation were removed. This removal procedure was repeated until the standard deviation of the remaining data points within the specific bin was smaller than 0.05 m. Third, of these remaining data points, only points that belong to bins which still had 50% or more of their data points after the standard deviation filter were kept to compute dune profiles (e.g., blue markers in Figure 3).

Next, the filtered bed level points were binned in time bins of 5 s and cross-shore spatial bins of 0.025 m to compute dune profiles every 5 s. Within each 5 s bin, data points that differed more than 0.05 m from the mean of the bin were removed. Next, a profile was computed using the mean of all bins excluding the 0.05 m outliers, and consequently smoothed by a uniform averaging window of 0.15 m long (black profile in Figure 3). The spatial extent of the data was different for each derived profile. Therefore, to make all profiles intercomparable for analysis, profiles were only kept if (a) the profiles extended at least up to an elevation of 4.5 m NAP (dune crest ≈ 5.5 m NAP), and (b) the profiles started at least at the cross-shore coordinate -16 m for the December storm and -13 m for the January storm. The differences in the minimal cross-shore value between both storms originated from the dune face being further landward in January. By increasing the minimum cross-shore value to -13 m, more profiles could be computed for the January data set.

Profiles were deemed reliable enough for analysis if they met two criteria. The first criterion was that the largest data gap between two data points that made up the profile was not larger than 0.50 m for the December storm and January storm between 14:00 and 16:00, and 1.50 m for the January storm from 16:00 onwards. Onwards from

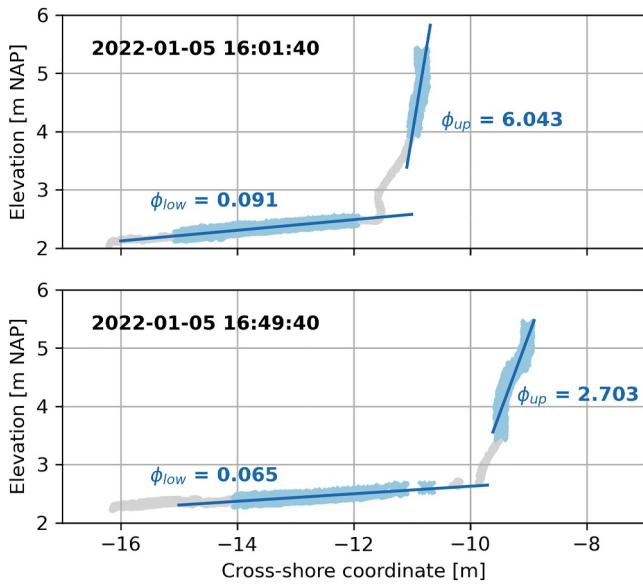


Figure 4. Derivation of ϕ_{up} and ϕ_{low} for two example profiles just before a slumping event during the January storm.

16:00, January 5, the distance from the lidar to the retreating dune face had increased considerably. As a consequence, the spatial resolution of the data near the dune face had decreased, and the maximum data gap needed to be increased to 1.50 m.

The second criterion was that each profile was only kept if the upper segment of the profile was stable in time. This criterion ensured that no profile would be developed for a 5 s bin during which a slumping event occurred. The stability of the upper segment was checked by computing the volume difference of the profile in question and the computed profile before it, or the computed profile after it, for the segment running from 3.50 to 4.50 m NAP. If this difference was smaller than $0.05 \text{ m}^3/\text{m}$, the criterion was met.

In the final processing step, the smoothed profiles were extended to the dune crest ($\approx 5.5 \text{ m NAP}$) of the initial profiles of both storms, if necessary. The mean \pm standard deviation of the extension distances of all December profiles was $0.04 \pm 0.15 \text{ m}$. For all January profiles, this was $0.08 \pm 0.14 \text{ m}$. The upward extensions toward the dune crest were linear and had a slope $\overline{\phi_{up}}$ of 4.984, where the slope is equal to the tangent of the angle of the (upper segment) of the dune profile ($4.984 = \tan 78.65^\circ$). The slope of 4.984 represents the average of the slopes calculated from linear fits applied to the upper data points within the 5 s profile bins before slumping events (Figure 4). Of all profiles, ϕ_{up} ranged from 2.229 to 8.182 (corresponding to angles of $65.84^\circ - 83.03^\circ$).

After this final processing step, all profiles started at the same cross-shore coordinate and extended to the same elevation, which made them suitable for an intercomparison of profile shapes and a determination of profile volumes.

All computed profiles were visually quality-controlled after the processing procedure, to (a) ensure that no water level points were detected as bed level points and used in the profile computation, and (b) ensure that the shape of the upper segment of profiles that required an extension compared well to profiles that did not require an extension. Overall, the December data set contained 249 profiles between 2021 and 12-01, 23:26, and 2021-12-02, 00:27. The January data set contained 858 profiles between 2022 and 01-05, 14:28, and 2022-01-05, 18:28.

3.2. Quantifying the Total Dune Volume and Erosion Rate From the Lidar-Derived Profiles

The total dune volume (V_{total} in m^3/m) was defined as the area within the lidar-derived profile cross-section above an elevation of 2 m NAP, between the cross-shore coordinate of the offshore boundary of the profiles (-16 m for the December and -13 m for the January storm) and -6 m . The lower elevation bound of 2 m NAP was used because all profiles were above this elevation. The landward cross-shore bound of -6 m was used because the dune crest was always seaward of this bound. Note that V_{total} , although computed as a lateral area within a profile cross-section, represents a volume per unit beach width in m^3/m assuming alongshore uniformity in the profile shape.

Throughout the storms, sediment is lost from V_{total} due to erosion of sediment at the dune base following from marine processes. The erosion rate (i.e., sand flux, q_{out} in $\text{m}^3/\text{m/s}$) is computed as

$$q_{out} = \frac{\Delta V_{total}}{\Delta t}, \quad (1)$$

where ΔV_{total} represents the total volume difference and Δt the time difference between subsequent profile cross-sections.

3.3. Quantifying Slumps From the Lidar-Derived Profiles

During slumping events, sediment slid down the dune face and was redistributed within the profile (Figure 1c). This redistribution did not necessarily result in a net difference of V_{total} . Therefore, all lidar-derived profiles were

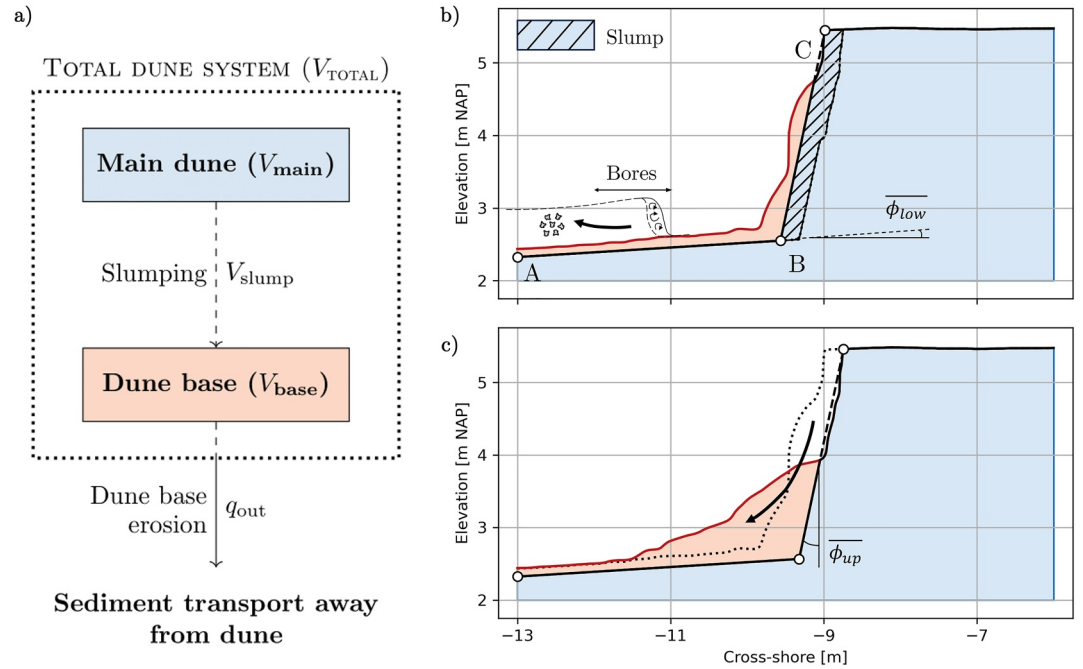


Figure 5. (a) The total dune volume was decomposed at each moment in time into a main dune volume (blue) and dune base volume (red) to quantify slumping volumes. Panels (b) and (c) display a schematic of the distinction between the main dune and dune base, for a profile before (16:49:40) and after (16:50:10) a slumping event in January. The volume of this slump is marked blue with a black pattern in panel (b).

separated into a main dune (V_{main} , blue in Figure 5) and dune base (V_{base} , red in Figure 5) to identify slumps and quantify slumping volumes,

$$V_{total} = V_{main} + V_{base}. \quad (2)$$

Slumping events (black arrow in Figure 5c) were identified by sudden changes in V_{main} , and the volume V_{slump} (m^3/m) of a slump was approximated as (hatched blue area in Figure 5b)

$$V_{slump} = V_{main, pre} - V_{main, post}, \quad (3)$$

where $V_{main, pre}$ and $V_{main, post}$ correspond to the pre- and post-slump main dune volumes, respectively. Over the course of both storms, V_{base} periodically increased due to slumping events (black arrow in Figure 5c), and continuously decreased due to persisting erosion rate of sediment at the dune base (q_{out} , Section 3.2) following from marine processes (thick black arrow in Figure 5b).

The main dune and dune base were separated by the path between points ABC (Figure 5b). Point A is located at the most seaward location of the profiles, with a cross-shore coordinate (x_A) equal to -16 m for the December storm and -13 m for the January storm. The elevation of A (z_A) is assumed equal to the minimum elevation at this cross-shore coordinate of all profiles recorded during the storm. Point C (with cross-shore coordinate x_C and elevation z_C) is the dune crest and retreats during the storm. Point B (with cross-shore coordinate x_B and elevation z_B) is defined as the intersection between the line of retreat of the dune toe, extended upward from A, and the line of failure of the dune face, extended downward from C (Figures 5b and 5c). The slope of the line of retreat is assumed equal to $\overline{\phi}_{low}$, which is 0.066 ($=\tan 3.78^\circ$). This slope was the average of the slopes calculated from linear fits applied to the lower data points within the 5 s profile bins before slumping events (Figure 4). Among all profiles, $\overline{\phi}_{low}$ ranged from 0.035 ($=\tan 2.00^\circ$) to 0.091 ($=\tan 5.20^\circ$). The slope of the line of failure is assumed equal to $\overline{\phi}_{up}$ ($=4.984$).

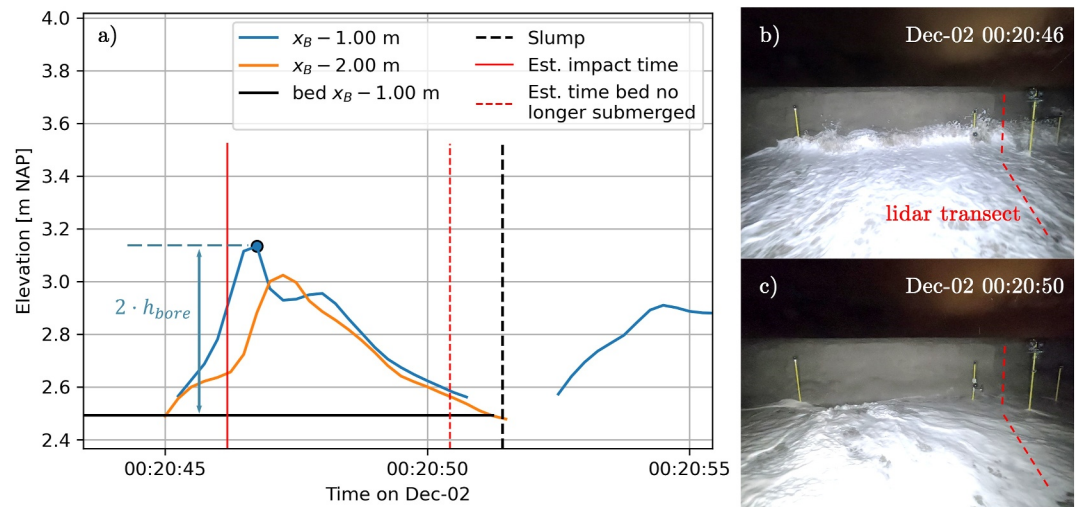


Figure 6. (a) Lidar water level time series during impact of the last wave before a slumping event on 2021-12-02, 00:20:51, 2 m (orange) and 1 m (blue) in front of point B. (b) Corresponding GoPro image of the estimated impact time in panel (a). (c) Corresponding GoPro image of the estimated time when the swash bore before the slumping event no longer submerged the bed at x_B . The bore height was approximated as half the height of the peak relative to the bed at the most onshore location ($x_B - 1.00$ m in this case).

3.4. Lidar-Derived Water Levels

Water level time series in close proximity to the dune face were computed by separating water level points from the unprocessed lidar point cloud. Points representing the water level were separated from the point cloud by using the derived location of the bed, based on the computed profiles.

First, all data points in the unprocessed lidar point cloud were binned in cross-shore direction with a bin width of 0.10 m. Within each spatial bin, points were regarded as water level points when they were minimally 0.05 m above the instantaneous bed level of the spatial bin, and minimally 0.10 m in front of the instantaneous dune face (in cross-shore direction). The locations of the instantaneous bed level and dune face were based on the lidar-derived dune profiles. Next, for each spatial bin, the water level points were converted to a time series of $\eta_L(t, x)$ by applying a Gaussian weighted moving average in time on the extracted water level points. The moving average had a width of 0.25 s, and the Gaussian window had a standard deviation of 0.25 s. The result is a time series of the water level for each 35- (December storm) or 50-min (January storm) burst at the location of each cross-shore bin, with a sampling frequency of 4 Hz.

3.5. Quantifying Wave Impact Force Based on the Water Level Time Series

The impact force of a bore on the dune face (F_{impact}) was estimated as (Cross, 1967; Erikson et al., 2007; Larson et al., 2004; Nishi & Kraus, 1996; Overton et al., 1988)

$$F_{\text{impact}} = \frac{1}{2} \cdot \rho \cdot h_{\text{bore}} \cdot u_{\text{bore}}^2, \quad (4)$$

with ρ the fluid density ($1,025 \text{ kg/m}^3$), h_{bore} the incident bore height, and u_{bore} the cross-shore velocity of the incident bore impacting the dune.

For bins near the dune face containing water level data, the lidar did not have a frontal view of the bore front (see Figure 6b), and interactions between the incident and reflected components prevented a direct estimation of h_{bore} (see Figure 6a: the peak at $x = x_B - 2.00$ m occurred later in time than at $x = x_B - 1.00$ m, indicating that the peaks correspond to the reflected component of the bore). Instead, the bore height was estimated as half the total crest elevation in the water level time series relative to the most recent instantaneous bed elevation, where we assumed full reflection (see blue in Figure 6a). The bore velocity was estimated as $\sqrt{g \cdot h_{\text{bore}}}$ (Cross, 1967; Erikson et al., 2007; Larson et al., 2004; Miller, 1968), where g is the gravitational acceleration.

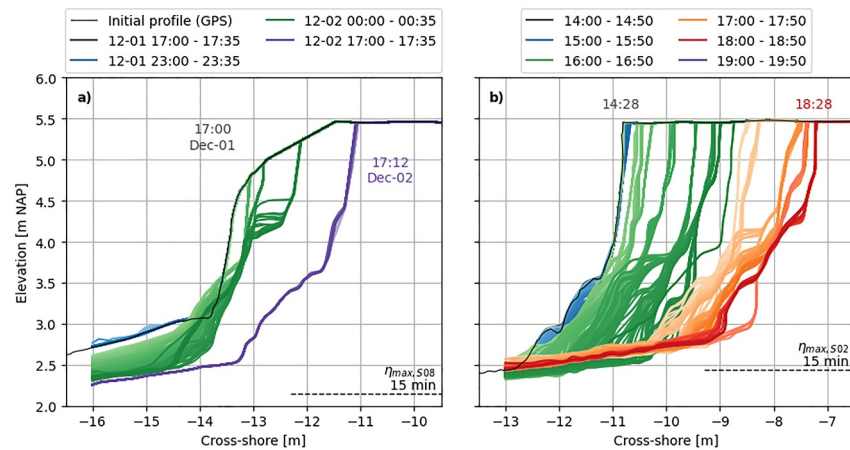


Figure 7. Derived profile cross-sections for the December storm (a) and January storm (b). The solid black lines represent the initial profiles based on measurements with a Real Time Kinematic Global Positioning System (RTK GPS). The dashed horizontal lines represent the maximum 15-min averaged water level at S08 (December) and S02 (January).

For the estimation of the bore height we used the water level time series as close to the dune face as possible (i.e., as close to x_B as possible). A total of 15 slumps (3 in December and 12 in January) with a volume exceeding $0.20 \text{ m}^3/\text{m}$ were identified during both storms. For the first 10 slumps (three in December and the first seven in January), the water level time series 1.00 m in front of x_B were used. For remaining slumps 11, 12–14, and 15, the water level time series at $x = x_B - 1.50 \text{ m}$, $x = x_B - 2.00 \text{ m}$, and $x = x_B - 3.00 \text{ m}$ were used, respectively. For these last five slumps, the dune crest had retreated substantially. This resulted in a coarser resolution of the lidar point cloud and lidar-derived water levels in close proximity to the dune face, and prevented us from using a water level time series closer to x_B .

The time of impact (red vertical solid line in Figure 6a) was estimated by using the time of the peak of the total elevation within the analyzed water level time series (e.g., blue dot at 00:20:46.75 for $x_B - 1.00 \text{ m}$ in Figure 6a), u_{bore} , and the known distance between the location of the time series and x_B (1.00 m for this example). These time estimations were validated using GoPro frames of the December storm. Figure 6b displays a GoPro frame during the estimated impact time (00:20:46), and 6c displays a GoPro frame when the cross-shore location at B was estimated to no longer be submerged by the swash bore (00:20:50). Both estimations are based on the lidar-derived water level time series at $x = x_B - 1.00 \text{ m}$.

4. Analysis and Results

4.1. General Behavior of the Dune Profiles

During the December storm, the bed level at the most seaward point of the profile cross-sections lowered 0.46 m from 2.72 to 2.26 m NAP (Figure 7a at $x = -16 \text{ m}$). This lowering primarily occurred during the initial stages of the storm, when waves began reaching and colliding with the dune face (2021-12-02, 00:00–00:10). The dune crest retreated 2.26 m in the cross-shore direction, from -13.31 m to -11.05 m . During the January storm, the bed level at the most seaward point of the profile cross-sections lowered during initial stages of the storm but returned to its original elevation at the end of the storm ($\approx 2.45 \text{ m}$ NAP, Figure 7b at $x = -13 \text{ m}$). Between 14:00 and 19:00, 2022-01-05, the dune crest retreated 3.69 m in the cross-shore direction, from -10.87 m to -7.18 m .

Figures 8 and 9 display the water level at S08 or S02 and z_B (Figures 8a and 9a), V_{total} (Figures 8b and 9b), V_{main} and x_C (Figures 8c and 9c), V_{base} (Figures 8d and 9d), and V_{slump} (Figures 8e and 9e) over the course of the December and January storms, respectively. The parameters V_{main} and x_C have been plotted in the same panel to display their dependence. These parameters are related through the dune height, that is, the elevation difference between B and C, where the elevation of B depends on ϕ_{up} and ϕ_{low} .

The eroded volumes of sediment from the total dune system were 5.43 and $9.12 \text{ m}^3/\text{m}$ for the December and January storms, respectively (Figures 8b and 9b). The erosion rate of the total dune sediments (q_{out} , Equation 1), which can be visualized as the slope of V_{total} in Figures 8b and 9b, differed during both storms and was not

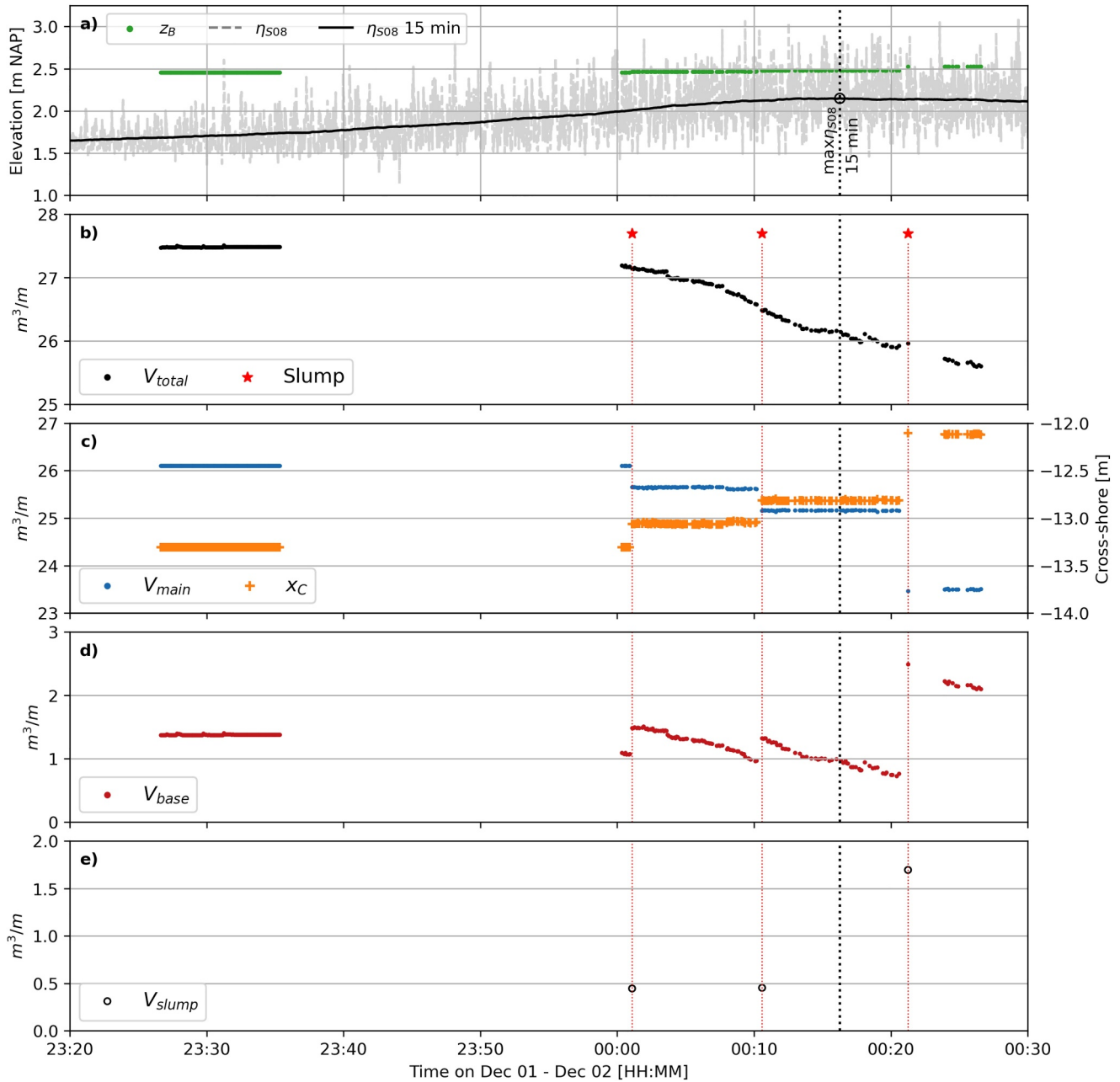


Figure 8. (a) Nearshore water levels based on the pressure sensor at S08 without (gray) and with a 15-min uniform moving average (black), during the December storm. Green dots represent the elevation of B. (b) V_{total} , (c) V_{main} (blue markers) and the cross-shore location of C (orange pluses), (d) V_{base} , and (e) V_{slump} for slumping events with a volume exceeding $0.20 \text{ m}^3/\text{m}$. The times at which the slumping events occurred are marked by the vertical dotted red lines in panels b–e.

constant. In January, V_{total} followed an S-shape curve, which suggests that q_{out} first increased and then decreased again. When comparing panels Figures 9a and 9b, it appears that this increase and decrease of q_{out} displays a similar trend as the 15-min averaged water level. This observation could not be validated for the December storm, because no profiles could be generated from the lidar data during the later stages of storm when the 15-min averaged water level lowered again (after 00:30 in Figure 8a). The relation between the 15-min averaged water level and q_{out} is further studied in Section 4.2.

A total of 3 slumping events with a volume exceeding $0.20 \text{ m}^3/\text{m}$ were identified in the December data set (Figure 8e). A total of 12 slumps exceeding $0.20 \text{ m}^3/\text{m}$ were identified in the January data set (Figure 9e). At least one slumping event on January 5 was not identified because it occurred between 16:50 and 17:00, during the

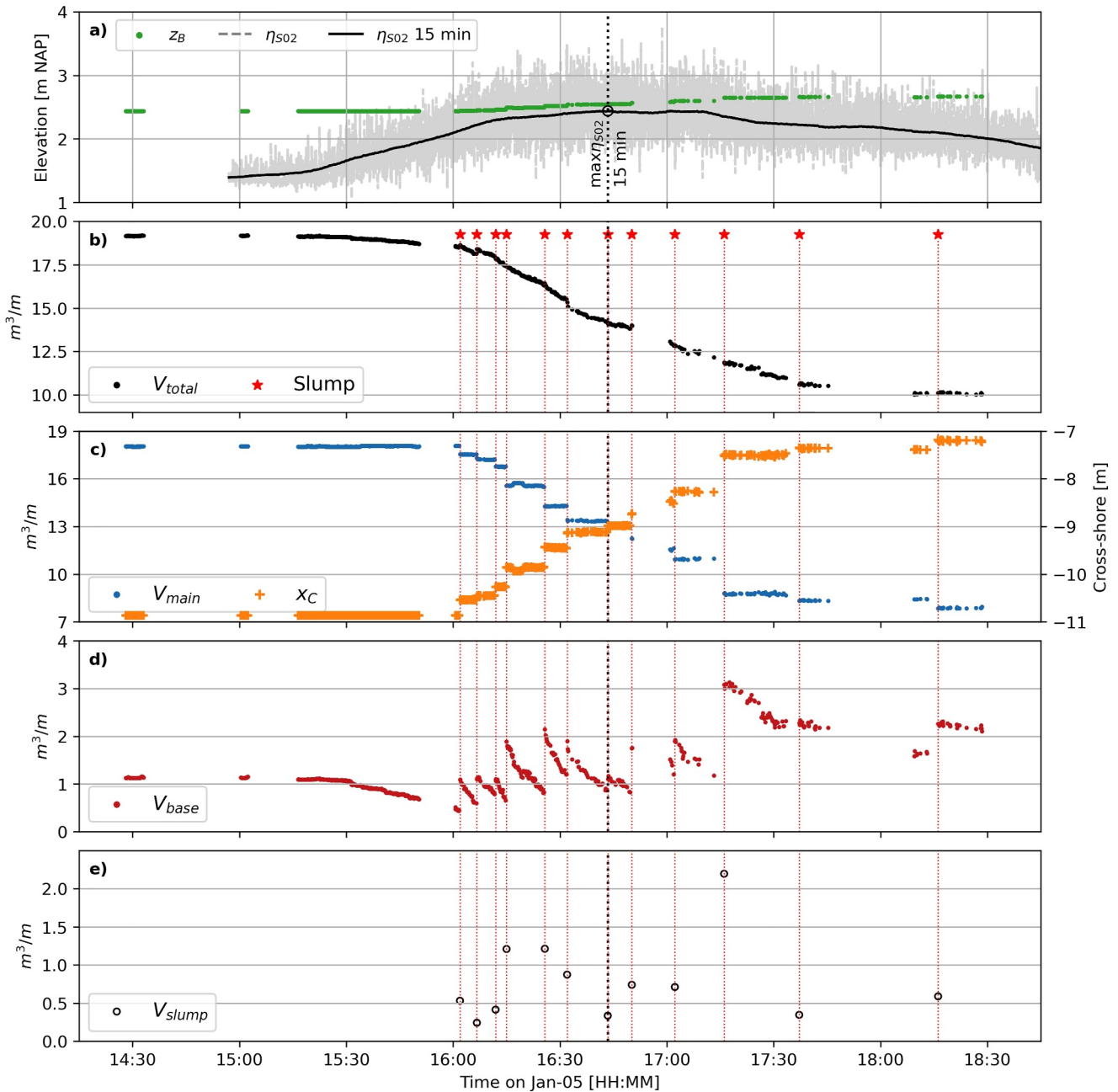


Figure 9. (a) Nearshore water levels based on the pressure sensor at S02 without (gray) and with a 15-min uniform moving average (black), during the January storm. Green dots represent the elevation of B. (b) V_{total} , (c) V_{main} (blue markers) and the cross-shore location of C (orange pluses), (d) V_{base} , and (e) V_{slump} for slumping events with a volume exceeding $0.20 \text{ m}^3/\text{m}$. The times at which the slumping events occurred are marked by the vertical dotted red lines in panels (b–e).

hourly 10-min span when the lidar was not logging (see difference in V_{main} and x_C in Figure 9c between 16:50 and 17:00).

The lower segment of the dune face (below approximately 4.0–4.5 m NAP, see Figure 7) of all profiles had a slope that gradually steepened between subsequent slumping events. The upper segment (above approximately 4.0–4.5 m NAP) was steeper, being nearly vertical or overhanging, and displayed less variability between slumping events. Only the pre-slump profiles of the first and last slump of the January storm experienced the formation of a notch at the dune toe (see Figure 4, upper panel). All 15 slumps experienced beam-type failure where the slump slid down a failure plane within the dune, regardless of the formation of a notch at the dune toe.

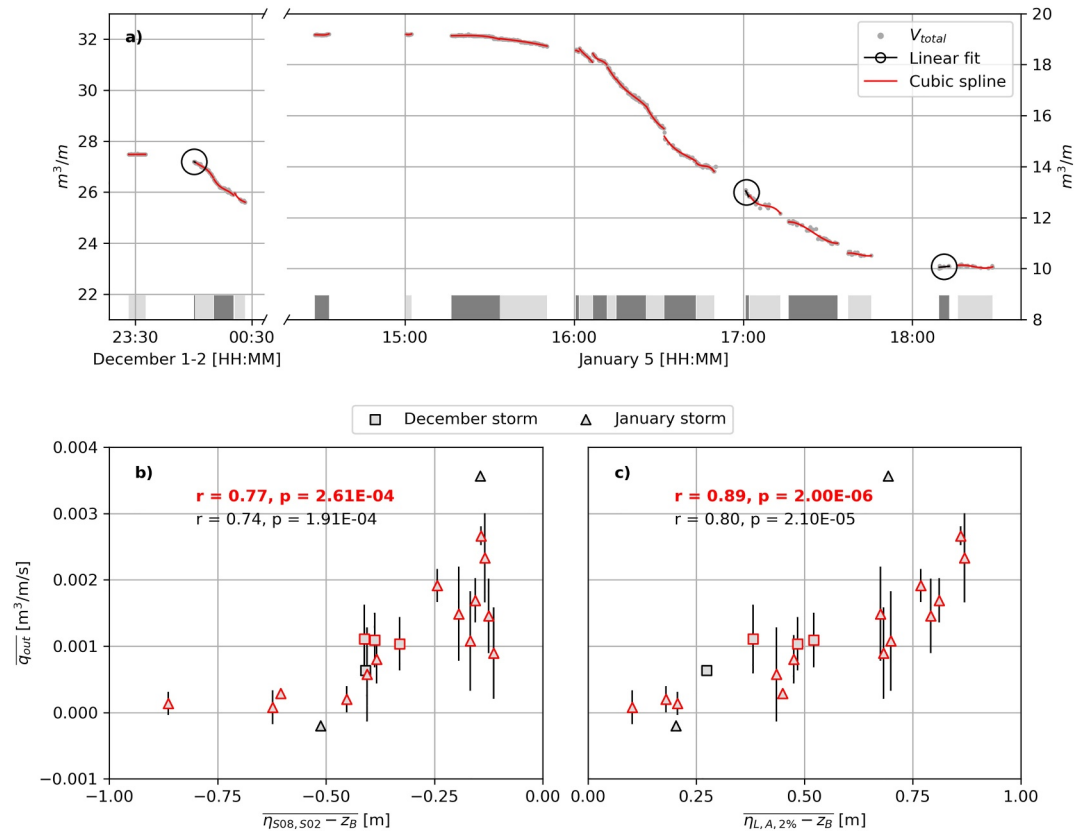


Figure 10. (a) Best fit cubic splines (red) and linear fits (encircled black) applied to V_{total} (gray dots, equal to black dots in Figures 8b and 9b), for the selected time intervals (gray bars above the time axis). Linear fits were applied when there were less than 10 profiles available in the time interval. Note that the December and January data have a vertical axis with identical scaling, but different values. (b) \bar{q}_{out} versus the time-averaged difference between the 15-min averaged water level, $\eta_{S08,S02}$, and z_B . (c) \bar{q}_{out} versus the time-averaged difference between $\eta_{L,A,2\%}$ and z_B . The black r values in panels (b) and (c) correspond to the correlation coefficients for all data points (red and black edges). The red values correspond to the correlation coefficients when time intervals with less than 10 profiles (black edges) were excluded in the computation. Vertical bars indicate ± 1 standard deviation of all gradients of each cubic spline in panel (a), used in the computation of \bar{q}_{out} .

4.2. Erosion Rate at the Dune Base

The erosion rate of sediment at the dune base (q_{out}) is computed using the change in time of the total dune volume (V_{total} , Equation 1). Figures 8b and 9b display several discontinuities in V_{total} over the course of the December and January storms. Large discontinuities are most likely due to slumping events, where slumped sediments did not necessarily remain within the lidar cross-section (i.e., sediment slumping sideways into or out of the lidar cross-section). For example, the discontinuity in V_{total} around 16:07 during the January storm (see Figure 9b) can probably be attributed to the 2nd slumping event in January. Minor discontinuities are likely due to small inaccuracies within the lidar-derived profile cross-sections, caused by bed level points not being identified in each consecutive 5 s lidar bin.

Possible effects due to discontinuities stemming from slumping events were excluded in the computation of q_{out} by separating the December and January storms into different time intervals, excluding slumping events, for which q_{out} was computed separately (dark and light gray bars in the lower part of Figure 10a). Smaller discontinuities attributed to sensor inaccuracies were removed by fitting a cubic spline through V_{total} within each time interval. For time intervals in which less than 10 profile cross-sections were available, a linear fit instead of a cubic spline was applied to V_{total} .

Time intervals were defined as (a) time intervals between consecutive slumps, given that both slumps occurred within the same lidar burst, (b) time intervals from the start of a lidar burst until the first slump of that burst, or the last slump of a lidar burst until the end of that burst, or (c) the entire duration of the lidar burst when no slumping

event occurred. The lidar burst between 15:00 and 16:00 on 2022-01-05, containing no slumping events, was separated into three time intervals. The 15-min averaged water level could not be regarded stationary within this 50-min interval, making a comparison between incident water levels and q_{out} difficult (see η_{S02} 15 min in Figure 9a).

The time-averaged erosion rate of the dune base sediments of each time interval, $\overline{q_{\text{out}}}$ (Equation 1, time-averaging is denoted by the bar), was approximated as the average gradient of the linear or cubic fit through V_{total} (Figure 10a). Figure 10b compares $\overline{q_{\text{out}}}$ with the time-averaged vertical difference between the 15-min averaged water level measured by the most shallow pressure sensor, $\eta_{\text{S08,S02}}$ (S08 in December and S02 in January, both are approximately 16.5 m in front of the dune), and the elevation of B , z_B . Time intervals during which incident waves did not reach the dune were excluded in the comparison (first interval in December, 23:27–23:35, and first two intervals in January, 14:28–14:33 and 15:00–15:02). Figure 10c compares $\overline{q_{\text{out}}}$ with the vertical difference between z_B and a 2% extreme water level ($\eta_{\text{L,A,2\%}}$). The parameter $\eta_{\text{L,A,2\%}}$ represents the water level of the lidar-derived water level timeseries at A that is exceeded 2% of the time. For example, if the time interval is 5 min long, it corresponds to a water level that is exceeded for a total duration of 6 s within that interval.

In general, both parameters correlated well with $\overline{q_{\text{out}}}$ ($r = 0.74, 0.80, p = 1.91\text{E}-04, 2.10\text{E}-05$ in Figures 10b and 10c). When data points based on fewer than 10 profiles are excluded from the computation, the correlation coefficients increased ($r = 0.77, 0.89, p = 2.61\text{E}-04, 2.00\text{E}-06$ in Figures 10b and 10c, red value). The difference between $\eta_{\text{S08,S02}}$ and z_B was negative for all time intervals (Figure 10a), which indicates that the 15-min averaged water level was below z_B , and wave runup and swash processes were responsible for water reaching the dune face (see gray timeseries Figures 8a and 9a).

Larson et al. (2004) relate the change of dune volume in time (i.e., erosion rate) to the square of a runup elevation relative to the dune toe elevation. In this experiment, the swash excursion in the nearshore exceeded the seaward extend of the lidar cross-shore field of view. As a consequence, not all individual wave runup events could be identified, and runup statistics (e.g., $R2\%$ after Stockdon et al., 2006) could not be calculated. If the runup is approximated with the parameter $\eta_{\text{L,A,2\%}} - z_B$ (Figure 10c), and the square of this value is correlated with q_{out} , the correlations slightly increase: $r = 0.80, p = 2.10\text{E}-05$ (including all data points) and $r = 0.91, p = 4.05\text{E}-07$ (excluding the data points based on fewer than 10 profiles).

4.3. Duration Between Slumps and Exact Slump Times

The duration between consecutive slumps varied over the course of both storms between 3 and 22 min (Figures 8e and 9e). GoPro images (e.g., Figures 1b and 6c) show that a slumping event occurred within the time frame when the dune face had a nearly vertical or overhanging profile. This observation is supported by the low dune base volumes (V_{base}) before each slumping event in Figures 8d and 9d.

The duration between slumping events was further analyzed for the time intervals in Figure 10a in which two slumping events occurred in the same lidar burst. Assuming that slumping events occur when V_{base} approaches zero, and V_{base} can only be replenished with the volume of individual slumping events (V_{slump}), from mass conservation it follows that the time-averaged erosion rate between the two slumping events ($\overline{q_{\text{out}}}$) is equal to $V_{\text{slump}}/\Delta t$, where V_{slump} is the volume of the first slumping event and Δt is the time difference between both events. Consequently, Δt can be approximated as $V_{\text{slump}}/\overline{q_{\text{out}}}$. Overall, this time approximation correlates significantly with the observed time between subsequent slumping events (Figure 11a, $r = 0.90, p = 1.71\text{E}-04$). Only the last identified slump of the January storm does not strongly display this relation (outlier in upper right corner in Figure 11a).

The strong correlation of the duration between slumping events and V_{slump} divided by $\overline{q_{\text{out}}}$ suggests that the frequency of slumping events is determined by how fast the sediment from the dune base, mainly replenished by the volume of previous slumps, is transported away from the dune. As a consequence, smaller slumps would be followed more rapidly by a new slump than larger slumps, under identical erosion rates.

Next, the exact timing of the 15 identified slumps is analyzed. Figure 11b displays the time difference between each slumping event and the approximated time of impact of the last bore before each slumping event. Overall, the time differences varied between 0.5 and 6 s, with one outlier at 16.75 s corresponding to the last slump of the January storm. On average, excluding the 16.75 s outlier, the time difference is 3 s.

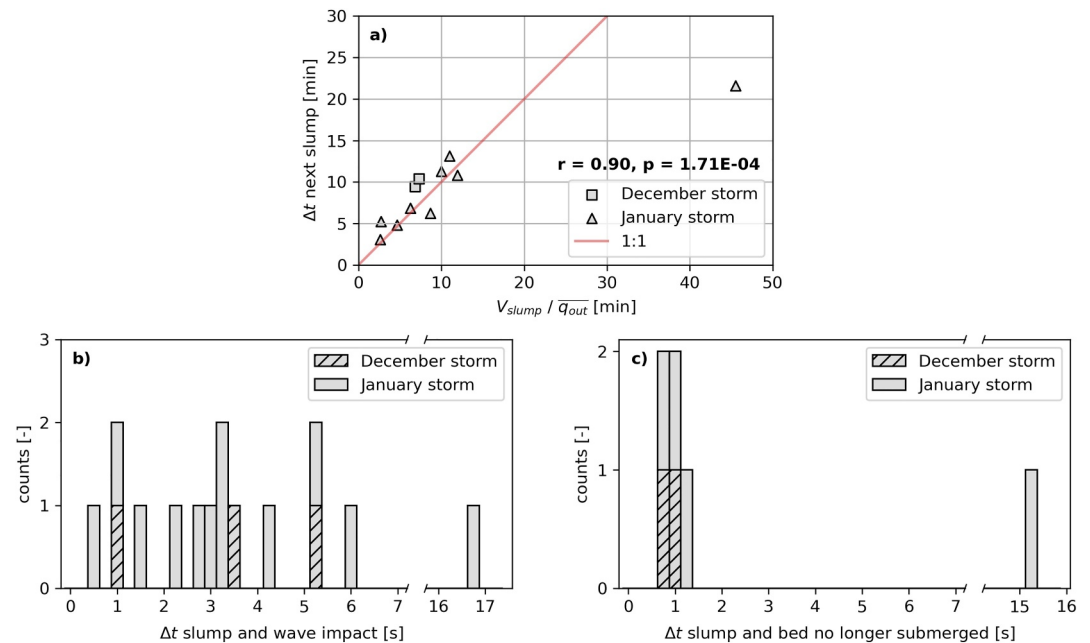


Figure 11. (a) Time until next slump (Δt) versus volume of the slump divided by the average erosion rate until the next slump (V_{slump}/\bar{q}_{out}) (b) Time between wave impact and the exact time at which the slumping event occurred. (c) Time between when the swash bore before the slumping event no longer submerged the cross-shore location of B (x_B) and the exact time at which a slumping event occurred. Data points in which the bed at x_B was still submerged are not displayed because no delay could be computed (9 of the 15 slumping events).

Figure 11c displays the time difference, if any, between each slumping event and the time when the last swash bore before the slumping event no longer submerged the cross-shore location of B (x_B). The time when the swash bore no longer submerged x_B was approximated similarly to the time of impact: The time at which the bed of the time series closest to B was no longer submerged by the swash bore was computed first, and then u_{bore} and the known distance between the location of the time series and x_B were used to approximate when the bed at x_B was no longer submerged (see red vertical dashed line in Figure 6a).

For 5 of the 15 slumps, the bed at x_B was no longer submerged by the swash bore approximately 0.75–1.25 s before the slumping event. For 1 slump (the last slump of the January storm), the bed at x_B was no longer submerged 15.25 s before the slumping event (right bar in Figure 11c). For the remaining 9 slumps, the bed at x_B was still submerged during the slumping event. For these 9 slumps, no time difference could be computed, and the water depth at the location of the time series closest to B ranged from 0.07 to 1.51 m, with an average of 0.63 m.

Overall, the majority of the slumping events occurred after the impact of the last bore and before the time when the bed in front of the dune was no longer submerged by this last bore, that is, when the water level in front of the dune was retreating.

4.4. Slump Volumes

The 15 identified slumps had volumes that ranged from 0.24 to 2.20 m^3/m , with a mean of 0.80 m^3/m . No clear pattern in the time evolution of the individual slump volumes could be observed (Figures 8e and 9e).

Slump volumes were analyzed by comparing the slump volumes (V_{slump}) with (a) the impact of the last bore before the slumping event (Figure 12a), (b) the number of wave impacts between consecutive slumping events, N (Figure 12b), (c) the cumulative impact force between consecutive slumping events (Figure 12c), and (d) the mean impact force (= cumulative impact force divided by N , Figure 12d). Figures 12b–12d only contain data points for the time intervals in which all impacts between slumping events could be identified. This is the case for the time intervals of Figure 10a in which two slumping events occurred in the same lidar burst. Overall, there was variability in the impact force of the last wave impact, the number of impacts before a slumping event, the

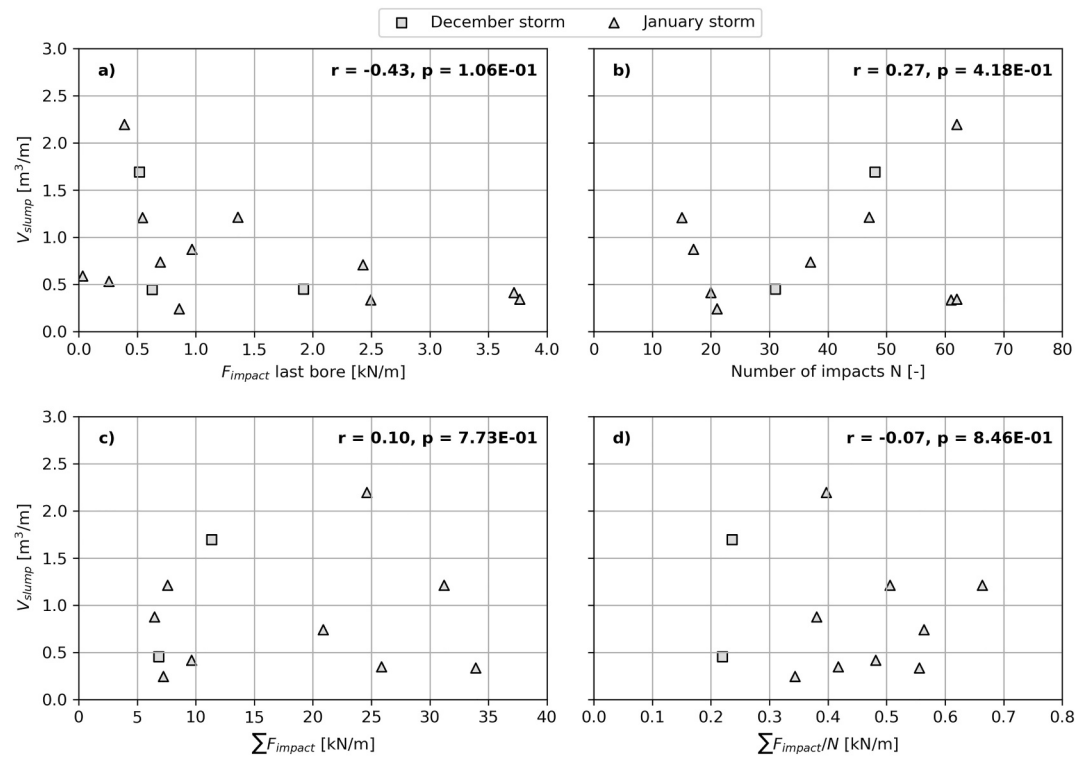


Figure 12. Individual slump volumes versus (a) the total impact force of the last wave before slumping, (b) the number of impacts between consecutive slumping events, N , (c) the cumulative impact force between consecutive slumping events, and (d) the mean impact force.

cumulative impact force for the different slumping events, and the mean impact force. No significant correlation could be identified between the slump volumes and the analyzed parameters.

Altogether, the lack of a distinct relation between slump volumes and wave impact suggests that slumps are not solely triggered by the hydrodynamic behavior outside the dune. Potentially, the dune geometry in combination with mechanisms related to soil mechanics inside the dune may play a role in determining the size of individual slumps (e.g., geotechnical properties of the dune sediments, internal shear stresses, failure planes, see Conti et al., 2024; Erikson et al., 2007; Overton et al., 1994; Palmsten & Holman 2011, 2012). Direct or indirect measurements of such properties are not available in the data set of this field experiment.

5. Discussion

This study presented novel hydrodynamic and morphodynamic data from a large-scale field experiment designed to study dune erosion rates and slumping processes. Lidar data were used to analyze the morphodynamic change of the dune profile, which was separated into a main dune and dune base to quantify slump volumes. Individual slumping events and the temporal variability of multiple slumping events over the course of two storms were analyzed, leading to new insights into slumping processes under naturally occurring hydrodynamic conditions. This section will first discuss the limitations of the lidar-derived profiles. Second, it will present the accuracy of the derived slump volumes, following from the separation of the dune profile into a main dune and dune base. Finally, it will present the implications of this study for wave impact models predicting dune erosion.

5.1. Limitations of the Lidar-Derived Profiles

The lidar provided elevation data only. Possible changes in the total dune volume (V_{total}) due to the changes in compaction during slumping events cannot be excluded. It is likely that the sediments from the main dune were more compacted than the slumped sediments at the dune base, which could lead to an apparent increase in total dune volume during a slumping event. In addition, possible changes in V_{total} during slumping events due to

sediment slumping sideways (i.e., in alongshore direction) into or out of the lidar cross-section cannot be excluded.

Overall, the average time between the last profile cross-section that could be generated before a slumping event, and the first profile cross-section that could be generated after a slumping event was 54 ± 72 s (where 72 s represents the standard deviation). The large time difference mainly originates from the final three slumps during the January storm. By then the distance from the lidar to the dune face had increased considerably, resulting in fewer profiles over time that could be generated following the filtering and processing technique explained in Section 3. When these three slumping event are excluded, the time difference is 19 ± 9 s. The differences in V_{total} , computed as V_{total} post-slump minus V_{total} pre-slump, was equal to -0.03 ± 0.17 m³/m. The difference excluding the last three slumping events was equal 0.02 ± 0.13 m³/m.

Possible effects due to sediment leaving or entering the lidar cross-section during slumping events were mitigated as much as possible by (a) separating the total storm into time intervals and excluding slumping events in the computation of q_{out} , and (b) computing the slumping volumes using changes in V_{main} . The sediments that make up V_{main} have not slumped yet. As a consequence, this volume could not be affected by sediment slumping to or from the lidar cross-section. Possible effects due to differences in compaction between the main dune and dune base could not be excluded in the analyses.

5.2. Accuracy of the Derived Slump Volumes

During slumping events, sediment slid down the dune face and was redistributed within the profile. This redistribution did not necessarily result in a net difference of the sediment volume of the total profile. In addition, the sliding down of sediment was not instantaneous and sometimes took several seconds. For example, the last slump in December continued sliding down the dune face for several minutes (darkest green profiles in Figure 7a). As a consequence, an accurate quantification of the individual slump volumes based on instantaneous profiles was not straightforward. A differentiation between a main dune and dune base was established, with the assumption that sediments were considered part of the slump volume once they left the main dune.

The boundary between the main dune and dune base was defined as the path *ABC* (Figure 5). The cross-shore coordinates and elevations of *A*, *B*, and *C* are important parameters in the differentiation between the main dune and dune base volumes. The point *A* was fixed, with a cross-shore coordinate of -16 m during the December storm and -13 m during the January storm. The elevation of *A* (z_A) was defined as the minimum elevation of all recorded profiles at the defined cross-shore coordinate of *A*.

By keeping the value of *A* fixed at the minimum bed level throughout each storm, the movement of sediment from the main dune to the dune base could only occur at the dune face, the region where slumping occurs. The actual bed level at *A* was sometimes higher in elevation than the definition for z_A , contributing to a larger dune base volume than reality. The additional contribution due to this actual bed level can be approximated as the elevation difference between the actual bed and z_A , times the cross-shore distance from *A* to *B*. In December, this volume contribution was on average 0.61 ± 0.34 m³/m (where 0.34 m³/m represents the standard deviation). In January, this was 0.27 ± 0.20 m³/m. The relatively larger contribution in December was due to the initial dune base reaching further seaward than x_A , outside the lidar cross-shore field of view (Figure 7). However, erosion rate and slump volume calculations should not be affected by the elevation discrepancy, because the elevation difference is similar in subsequent profiles (e.g., red shaded areas in Figures 5b and 5c).

The location of *C* changed over the course of the storm due to the dune crest retreating. Point *C* determined the size of the individual slumps due to its movement. The location of *C* was determined by the point with the highest elevation within the profile, and an extension to the dune crest following the slope of $\overline{\phi_{\text{up}}}$, if necessary. The mean \pm standard deviation of the extension distances of all December profiles was 0.04 ± 0.15 m. For all January profiles, this was 0.08 ± 0.14 m. The mean \pm standard deviation profile extension distances within the time intervals spanned by the data in Figure 10a was less than 0.12 ± 0.03 m, with the exception of four time intervals: 2021-12-02 after 00:20:51 (mean \pm standard deviation extension distance of 0.63 ± 0.01 m due to L3 only capturing the dune face up to 5.0 m NAP; Figure 3c); 2022-01-05 between 16:11:50 and 16:14:53 (0.60 ± 0.05 m); 2022-01-05 between 16:14:53 and 16:25:45 (0.35 ± 0.20 m); and 2022-01-05 between 17:02:07 and 17:15:16 (0.27 ± 0.04 m). However, the standard deviation within the time intervals of Figure 10a of the cross-shore position of *C* remained small (less than 0.03 m for all four time intervals). This suggests that the influence of

the differences in the extension distances of the profiles on the cross-shore position of C , and consequently on the slump volumes, remained small. Therefore, extrapolating the profiles to the dune crest following the slope of $\overline{\phi}_{up}$ is assumed viable for carrying out dune volume analyses.

The standard deviation of the location of C , and consequently B (Figure 5c), within the time intervals spanned by the data shown in Figure 10a, translated to a standard deviation of the pre- and post slump main dune volumes of 0.01–0.09 m³/m. As a consequence, the computed individual slump volumes have a standard deviation equal to the sum of the standard deviations of the pre- and post main dune volumes. This resulted in standard deviations of the slump volumes ranging from 1% to 14% of the total slump volume, with a mean of 6.2%.

The definition of B required knowledge of (a) the average slope $\overline{\phi}_{up}$ of the line of failure within the dune along which the sediments slumped down, and (b) the average slope $\overline{\phi}_{low}$ of the line of retreat of the dune toe. Different values of the slopes of both lines lead to differences in computed slump volumes. Both lines gradually became visible when sediments at the dune base were transported away from the dune. However, because not all dune base sediments were always washed away before a new slump slid down, the lower part of the line of failure and the upper part of the line of retreat were not always visible.

The values of $\overline{\phi}_{up}$ and $\overline{\phi}_{low}$ were estimated using the separated bed level points just before slumping events, during which the greatest segments of both lines were visible (Figure 4). Possible errors in $\overline{\phi}_{up}$ should not significantly influence slump volume calculations (Equation 3), because the pre- and post-slump profiles use the same value of $\overline{\phi}_{up}$. Possible errors in $\overline{\phi}_{low}$ lead to different elevations of B (Figure 5b), which could introduce error in the computation of the slump volumes. The range of the elevations of B due to differences in $\overline{\phi}_{low}$ was approximated using the distance between B and A , and the variability of ϕ_{low} , which ranged from 0.035 to 0.091. The least favorable situation combined a ϕ_{low} of 0.035 with the largest observed distance between B and A (5.26 m in January). This led to an elevation of B that was 0.16 m lower than the elevation of B computed as described in Section 3.3, which had a ϕ_{low} of 0.066. The least favorable situation led to a deviation of 6% of the total slump volume as computed in Section 3.3, based on the total height of the slump (distance from B to C in Figure 5b). Overall, the average deviation of all slumps was 4% of the slump volume as computed in Section 3.3.

Altogether, when the possible deviations of the computed slump volumes due to (a) the standard deviation of the position of C and (b) a possible error in $\overline{\phi}_{low}$ are combined, the slump that occurred at 17:37, January 5, had the largest possible deviation of the computed value. This deviation was equal to 15% of the total slump volume as computed in Section 3.3. The average combined deviation of all 15 slumps was 8% of the slump volume as computed in Section 3.3.

The assumption of single value for $\overline{\phi}_{up}$ for all profiles assumes the slope of the failure plane downward from C is identical for all slumping events. However, this assumption could not be validated, because neither the internal structure of the dune nor possible shapes of failure planes were measured. To better define slumping volumes and failure planes, further experimental studies into geotechnical properties (Conti et al., 2024; Overton et al., 1994), internal stability (Palmsten & Holman, 2011), and failure planes (Erikson et al., 2007) within dunes, in conjunction with continuous measurement of dune profile evolution, will be of added value.

5.3. Implications for Wave Impact Models Predicting Dune Erosion

Several dune erosion models relate the amount of dune erosion to the impact of incoming waves (Erikson et al., 2007; Fisher et al., 1987; Larson et al., 2004; Overton et al., 1988, 1994). The principles of wave impact theory were developed in Fisher and Overton (1984) and validated through laboratory tests in Overton et al. (1988). In these tests, a single bore impacted a vertical dune face and resulted in a slump dropping down. The experiment results displayed a linear relation between the impact force of the bore and the volume of the slumping event.

In this study, slumping processes were studied over the course of a storm, rather than for individual events. Slumping events likely occurred when sediments at the dune base from previous slumps were nearly depleted by the persisting erosion rate. It appears that once sediments slumped down, they provided temporarily stability to the dune face, protected it against direct wave attack, and temporarily prevented new slumping events from occurring. As a result, the morphodynamic behavior of the upper dune face and dune crest was steered by the morphodynamic behavior of the slumped sediments at the dune base.

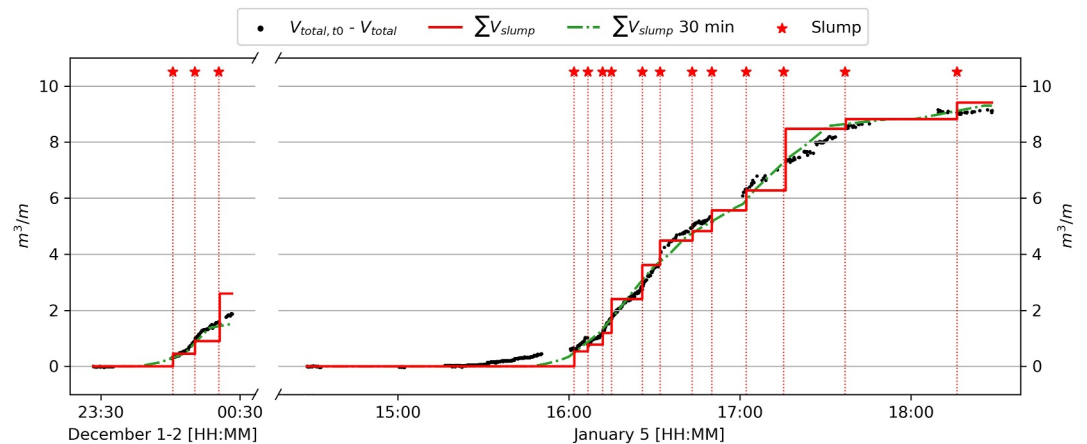


Figure 13. Cumulative slump volume ($\sum V_{slump}$, solid red) and volume difference between the initial total dune volume ($V_{total, t0}$) and the total dune volume (V_{total}) during the storm (black). Red vertical lines indicate the exact time of slumping events. The green dash-dotted curve displays the 30-min averaged cumulative slump volume.

Consequently, the cumulative volume of slumped sediments (Figure 13, red solid curve) fluctuates around the decrease of the total dune volume (V_{total}) due to the persisting erosion rate of sediments at the dune base (Figure 13, black markers). The magnitude of the fluctuations depends on the size of the individual slumps. Time-averaging this cumulative slumped volume removes these fluctuations, and increases similarities between the cumulative slumped volume and the decrease in V_{total} (Figure 13, green dash-dotted curve).

Altogether, the observations of this study suggest that the total (i.e., cumulative) dune erosion volume during a storm can be replicated using estimates of the volumes of individual slumps, when these estimates account for the delay between slumping events due to the presence of slumped sediments at the dune base. No clear relationship could be established between the hydrodynamics outside of the dune and the volume of individual slumping events, indicating that the slump volumes likely relate to internal soil mechanics and geotechnical properties of the dune sediments. The presence and morphodynamic behavior of slumped sediments at the dune base depended on the erosion rate of these sediments, which correlated significantly with the square of the elevation difference between the dune base and the incident water level that was exceeded 2% of the time.

Given that current dune erosion models commonly use hydrodynamic input parameters, it might be more practical to replicate the morphodynamic processes at the dune base instead of the geotechnical processes of the upper dune face. If we assume that the morphodynamic behavior at the dune base steers the morphodynamic behavior of the upper dune face, dune erosion models may achieve more accurate results when they compute the erosion rate of the dune base sediments based on the incident hydrodynamics, and relate this erosion rate to a time-averaged erosion rate of the dune face due to slumping.

6. Conclusions

This study presented and analyzed data of a detailed field experiment to study dune erosion rates and slumping processes. Two artificial unvegetated dunes were constructed above the high water line and experienced dune erosion in the swash-dune collision regime during two storms. Hydrodynamics and dune morphology were measured using a line-scanning lidar system, GoPro cameras, and pressure sensors. The priorities of the analysis focused on hydrodynamic processes seaward of the dune, as well as subsequent dune erosion rates and slumping processes. Analysis encompassed (a) the behavior and change of the total dune profile over the course of both storms, (b) the erosion rate at the dune base, (c) the slumping frequency and the exact time at which a slumping event occurred, and (d) the volumes of individual slumps.

The measured erosion rate of the dune base sediments correlated well with the elevation difference between the dune base and (a) the 15-min averaged water level recorded approximately 16.5 m in front of the dune ($r = 0.77$, $p = 2.61E-04$), and (b) the total water level, recorded approximately 5–6 m in front of the dune face that was exceeded for 2% of the time ($r = 0.89$, $p = 2.00E-06$). Erosion rates increased when these two indicators of the

water level increased. The largest correlation with the erosion rate was found for the square of the elevation difference between the dune base and the total water level that was exceeded for 2% of the time ($r = 0.91$, $p = 4.05E-07$). At approximately 16.5 m in front of the dune face, the 15-min averaged water levels were always below the elevation of the dune base, suggesting that wave motion and swash were responsible for water reaching the dune face.

The slumping events that occurred during both storms likely occurred when sediments at the dune base from previous slumps were nearly depleted by the persisting erosion rate. A strong relation was found between the elapsed time between consecutive slumps and the volume of the first slump divided by the mean erosion rate between the consecutive slumps ($r = 0.90$, $p = 1.71E-04$). As a consequence, smaller slumps (by volume) were followed more rapidly by a new slump than larger slumps, under similar erosion rates. The majority of the slumping events occurred after the impact of the last bore and before the time when the bed in front of the dune was no longer submerged by this last bore (i.e., when the instantaneous water level in front of the dune was retreating). A clear relationship could not be established between hydrodynamics seaward of the dune and the volume of individual slumps.

Overall, for the events and conditions studied here, the results suggest that slumping events depend on the amount of sediments present at the dune base and the erosion rate of these dune base sediments. This indicates that the morphodynamic behavior of the upper dune face and dune crest is steered by the morphodynamic behavior at the dune base. Consequently, dune erosion models may achieve more accurate results when they compute the erosion rate of the dune base sediments based on the incident hydrodynamics, and relate this erosion rate to an erosion rate of the dune face due to slumping. In this study, the erosion rate of the dune base sediments correlated significantly with the square of the elevation difference between the dune base and the incident water level that was exceeded 2% of the time. Thus, to accurately assess the risks sandy coastlines face during storm surges using dune erosion models, an accurate estimation of water levels and erosion rates at the dune base can enhance the capabilities to quantify the impact of these events.

Data Availability Statement

The data on which this article is based are openly available in van Wiechen, Rutten, et al. (2023) and Rutten et al. (2024b). The accompanying data papers are van Wiechen et al. (2024) and Rutten et al. (2024a), respectively.

Acknowledgments

The RealDune-REFLEX experiments are part of the RealDune and Reflex projects. Both projects were funded by TKI (Top consortium for Knowledge and Innovation) Delta Technology. The RealDune consortium exists out of Delft University of Technology, Rijkswaterstaat (the Dutch Ministry of Infrastructure and Water Management), STOWA (the Dutch Waterboards), Deltares, Arcadis, and Witteveen + Bos. The REFLEX consortium exists out of Delft University of Technology, Rijkswaterstaat, Deltares, Stichting Zawabas, Witteveen + Bos, Arcadis, and Nortek. The dunes of the experiment were constructed by Boskalis. The authors thank Christine Baker, Jantien Rutten, and Katherine Anarde for their valuable input on the performed analyses of this study. In addition, the authors thank the reviewers for their constructive, clear, and detailed comments.

References

- Bond, H., Wengrove, M., Puleo, J., Pontiki, M., Evans, T. M., & Feagin, R. A. (2023). Beach and dune subsurface hydrodynamics and their influence on the formation of dune scarps. *Journal of Geophysical Research: Earth Surface*, 128(12), 1–17. <https://doi.org/10.1029/2023JF007298>
- Carter, R. W. G., Hesp, P., & Nordstrom, K. (1990). Erosional landforms in coastal dunes. *Coastal Dunes: Form and Process*, 217–250.
- Castelle, B., Mariou, V., Bujan, S., Splinter, K. D., Robinet, A., Sénéchal, N., & Ferreira, S. (2015). Impact of the winter 2013–2014 series of severe Western Europe storms on a double-barred sandy coast: Beach and dune erosion and megacusp embayments. *Geomorphology*, 238, 135–148. <https://doi.org/10.1016/j.geomorph.2015.03.006>
- Conti, S., Splinter, K., Booth, E., Djadjiguna, D., & Turner, I. (2024). Observations on the role of internal sand moisture dynamics in wave-driven dune face erosion. *Geomorphology*, 462(April), 109331. <https://doi.org/10.1016/j.geomorph.2024.109331>
- Cross, R. H. (1967). Tsunami surge forces. *Journal of the Waterways and Harbors Division*, 93(4), 201–231. <https://doi.org/10.1061/jwheau.0000528>
- de Winter, R. C., Gongriep, F., & Ruessink, B. G. (2015). Observations and modeling of alongshore variability in dune erosion at Egmond aan Zee, The Netherlands. *Coastal Engineering*, 99, 167–175. <https://doi.org/10.1016/j.coastaleng.2015.02.005>
- Erikson, L., Larson, M., & Hanson, H. (2007). Laboratory investigation of beach scarp and dune recession due to notching and subsequent failure. *Marine Geology*, 245(1–4), 1–19. <https://doi.org/10.1016/j.margeo.2007.04.006>
- Feagin, R. A., Innocenti, R. A., Bond, H., Wengrove, M., Huff, T. P., Lomonaco, P., et al. (2023). Does vegetation accelerate coastal dune erosion during extreme events? *Science Advances*, 9(24), 1–10. <https://doi.org/10.1126/sciadv.adg7135>
- Fisher, J. S., & Overton, M. F. (1984). Numerical model for dune erosion due to wave uprush. *Proceedings of the Coastal Engineering Conference*, 2(2), 1553–1558. <https://doi.org/10.1061/9780872624382.106>
- Fisher, J. S., Overton, M. F., & Chisholm, T. (1987). Field measurements of dune erosion. *Proceedings of the Coastal Engineering Conference*, 2(11), 1107–1115. <https://doi.org/10.1061/9780872626003.082>
- Gharagozlou, A., Dietrich, J. C., Karanci, A., Luettich, R. A., & Overton, M. F. (2020). Storm-driven erosion and inundation of barrier islands from dune-to region-scales. *Coastal Engineering*, 158(June 2019), 103674. <https://doi.org/10.1016/j.coastaleng.2020.103674>
- Kobayashi, N., Buck, M., Payo, A., & Johnson, B. D. (2009). Berm and dune erosion during a storm. *Journal of Waterway, Port, Coastal, and Ocean Engineering*, 135(1), 1–10. [https://doi.org/10.1061/\(asce\)0733-950x\(2009\)135:1\(1\)](https://doi.org/10.1061/(asce)0733-950x(2009)135:1(1))
- Larson, M., Erikson, L., & Hanson, H. (2004). An analytical model to predict dune erosion due to wave impact. *Coastal Engineering*, 51(8–9), 675–696. <https://doi.org/10.1016/j.coastaleng.2004.07.003>

- Leaman, C. K., Harley, M. D., Splinter, K. D., Thrane, M. C., Kinsela, M. A., & Turner, I. L. (2021). A storm hazard matrix combining coastal flooding and beach erosion. *Coastal Engineering*, 170, 104001. <https://doi.org/10.1016/j.coastaleng.2021.104001>
- Masselink, G., Scott, T., Poate, T., Russell, P., Davidson, M., & Conley, D. (2016). The extreme 2013/2014 winter storms: Hydrodynamic forcing and coastal response along the southwest coast of England. *Earth Surface Processes and Landforms*, 41(3), 378–391. <https://doi.org/10.1002/esp.3836>
- Miller, R. L. (1968). Experimental determination of run-up of undular and fully developed bores. *Journal of Geophysical Research*, 73(14), 4497–4510. <https://doi.org/10.1029/JB073i014p04497>
- Nishi, R., & Kraus, N. C. (1996). Mechanism and calculation of sand dune erosion by storms. *Coastal Engineering Proceedings*, 1(25). <https://doi.org/10.9753/icce.v25.%25p>
- Nishi, R., Sato, M., & Wang, H. (1994). Field observation and numerical simulation of beach and dune scarps. *Coastal Engineering Proceedings*, 1(24), 2434–2448. <https://doi.org/10.1061/9780784400890.177>
- O'Connor, C. S., & Mieras, R. S. (2022). Beach profile, water level, and wave runup measurements using a standalone line-scanning, low-cost (LLC) LiDAR system. *Remote Sensing*, 14(19), 4968. <https://doi.org/10.3390/rs14194968>
- O'Dea, A., Brodie, K. L., & Hartzell, P. (2019). Continuous coastal monitoring with an automated terrestrial lidar scanner. *Journal of Marine Science and Engineering*, 7(2), 37. <https://doi.org/10.3390/JMSE7020037>
- Overton, M. F., Fisher, J. S., & Young, M. A. (1988). Laboratory investigation of dune erosion. *Journal of Waterway, Port, Coastal, and Ocean Engineering*, 114(3), 367–373. [https://doi.org/10.1061/\(asce\)0733-950x\(1988\)114:3\(367\)](https://doi.org/10.1061/(asce)0733-950x(1988)114:3(367))
- Overton, M. F., Pratikto, W. A., Lu, J. C., & Fisher, J. S. (1994). Laboratory investigation of dune erosion as a function of sand grain size and dune density. *Coastal Engineering*, 23(1–2), 151–165. [https://doi.org/10.1016/0378-3839\(94\)90020-5](https://doi.org/10.1016/0378-3839(94)90020-5)
- Palmsten, M. L., & Holman, R. A. (2011). Infiltration and instability in dune erosion. *Journal of Geophysical Research*, 116(10), C10030. <https://doi.org/10.1029/2011JC007083>
- Palmsten, M. L., & Holman, R. A. (2012). Laboratory investigation of dune erosion using stereo video. *Coastal Engineering*, 60(1), 123–135. <https://doi.org/10.1016/j.coastaleng.2011.09.003>
- Roelvink, D., McCall, R., Mehvar, S., Nederhoff, K., & Dastgheib, A. (2018). Improving predictions of swash dynamics in XBeach: The role of groupiness and incident-band runup. *Coastal Engineering*, 134, 103–123. <https://doi.org/10.1016/j.coastaleng.2017.07.004>
- Roelvink, D., Reniers, A., van Dongeren, A., van Thiel de Vries, J., McCall, R., & Lescinski, J. (2009). Modelling storm impacts on beaches, dunes and barrier islands. *Coastal Engineering*, 56(11–12), 1133–1152. <https://doi.org/10.1016/j.coastaleng.2009.08.006>
- Ruggiero, P., Komar, P. D., McDougal, W. G., Marra, J. J., & Beach, R. A. (2001). Wave runup, extreme water levels and the erosion of properties backing beaches. *Journal of Coastal Research*, 17(2), 407–419.
- Rutten, J., Tissier, M., van Wiechen, P., Zhang, X., de Vries, S., Reniers, A., & Mol, J.-W. (2024a). Continuous wave measurements collected in intermediate depth throughout the North sea storm season during the RealDune/REFLEX experiments. *Data*, 9(5), 70. <https://doi.org/10.3390/data9050070>
- Rutten, J., Tissier, M. F., van Wiechen, P., Zhang, X., de Vries, S., Reniers, A., & Mol, J.-W. (2024b). Data collection underlying the publication: Continuous wave measurements collected in intermediate depth throughout the North sea storm season during the RealDune/REFLEX experiments [Dataset]. *4TU.ResearchData*. <https://doi.org/10.4121/233f11ff-7804-4777-8b32-92c4606e56d8>
- Sallenger, A. H. (2000). Storm impact scale for barrier islands. *Journal of Coastal Research*, 16(3), 890–895.
- Schweiger, C., Kaehler, C., Koldrack, N., & Schuetttrumpf, H. (2020). Spatial and temporal evaluation of storm-induced erosion modelling based on a two-dimensional field case including an artificial unvegetated research dune. *Coastal Engineering*, 161, 103752. <https://doi.org/10.1016/j.coastaleng.2020.103752>
- Steezel, H. J. (1993). *Cross-shore transport during storm surges*. (Doctoral dissertation). Delft University of Technology. <https://doi.org/10.1061/9780872627765.147>
- Stive, M. J. F., de Schipper, M. A., Luijendijk, A. P., Aarninkhof, S. G., van Gelder-Maas, C., van Thiel de Vries, J. S., et al. (2013). A new alternative to saving our beaches from sea-level rise: The sand engine. *Journal of Coastal Research*, 29(5), 1001–1008. <https://doi.org/10.2112/JCOASTRES-D-13-00070.1>
- Stockdon, H. F., Holman, R. A., Howd, P. A., & Sallenger, A. H. (2006). Empirical parameterization of setup, swash, and runup. *Coastal Engineering*, 53(7), 573–588. <https://doi.org/10.1016/j.coastaleng.2005.12.005>
- van Bemmelen, C. W., de Schipper, M. A., Darnall, J., & Aarninkhof, S. G. (2020). Beach scarp dynamics at nourished beaches. *Coastal Engineering*, 160, 103725. <https://doi.org/10.1016/j.coastaleng.2020.103725>
- van Gent, M. R., van Thiel de Vries, J. S., Coeveld, E. M., de Vroeg, J. H., & van de Graaff, J. (2008). Large-scale dune erosion tests to study the influence of wave periods. *Coastal Engineering*, 55(12), 1041–1051. <https://doi.org/10.1016/j.coastaleng.2008.04.003>
- van Thiel de Vries, J. S. M., Clarke, L. B., Aarninkhof, S. G., Coeveld, E. M., Holman, R. A., Palmsten, M. L., et al. (2007). Interaction of dune face and swash zone. In *Coastal sediments '07—Proceedings of 6th international symposium on coastal engineering and science of coastal sediment processes* (pp. 1975–1987). American Society of Civil Engineers. [https://doi.org/10.1061/40926\(239\)155](https://doi.org/10.1061/40926(239)155)
- van Thiel de Vries, J. S. M., van Gent, M. R., Walstra, D. J., & Reniers, A. J. (2008). Analysis of dune erosion processes in large-scale flume experiments. *Coastal Engineering*, 55(12), 1028–1040. <https://doi.org/10.1016/j.coastaleng.2008.04.004>
- van Wiechen, P., de Vries, S., Reniers, A., & Aarninkhof, S. (2023a). Dune erosion during storm surges: A review of the observations, physics and modelling of the collision regime. *Coastal Engineering*, 186, 104383. <https://doi.org/10.1016/j.coastaleng.2023.104383>
- van Wiechen, P., Rutten, J., de Vries, S., Tissier, M., Mieras, R., Anarde, K., et al. (2024). Measurements of dune erosion processes during the RealDune/REFLEX experiments. *Scientific Data*, 11(1), 421. <https://doi.org/10.1038/s41597-024-03156-9>
- van Wiechen, P., Rutten, J., de Vries, S., Tissier, M., Mieras, R., Anarde, K., et al. (2023b). Nearshore coastal measurements of calm, moderate, and storm conditions at two artificial dunes along the Dutch Coast during the RealDune/REFLEX experiments. [Dataset]. *4TU.ResearchData*. <https://doi.org/10.4121/0a05d041-00b6-4e8e-a5c5-70e624ea720b>
- Vellinga, P. (1978). *Duinafslag ten gevolge van de stormvloed op 3 januari 1976; Toetsing van de Voorlopige Richtlijn*. (Tech. Rep.). Waterbouwkundig Laboratorium.
- Vellinga, P. (1986). *Beach and dune erosion during storm surges*. (Doctoral dissertation). Delft University of Technology. Retrieved from <http://resolver.tudelft.nl/uuid:eb7a4d20-86d2-469a-932a-dec0518274bb>
- Watermanagementcentrum Nederland. (2021). *Stormvloedflits 2021-05 van 1 December 2021*. (Tech. Rep.). Rijkswaterstaat. Retrieved from <https://open.rijkswaterstaat.nl/open-overheid/onderzoeksrapporten>
- Watermanagementcentrum Nederland. (2022). *Stormvloedflits 2022-01 Van 4 en 5 januari 2022*. (Tech. Rep.). Rijkswaterstaat. Retrieved from <https://open.rijkswaterstaat.nl/open-overheid/onderzoeksrapporten>